Physics in Medicine & Biology



# Absorbed and effective dose estimates in HR-pQCT of the distal radius and tibia: virtual dosimetry with a GPU-accelerated Monte Carlo code



IOP Publishing Phys. Med. Biol. 70 (2025) 095005 https://doi.org/10.1088/1361-6560/adc9f6

Physics in Medicine & Biology

IPEM Institute of Physics and Engineering in Medicine

OPEN ACCESS

RECEIVED
6 November 2024

REVISED
24 March 2025

ACCEPTED FOR PUBLICATION
7 April 2025

PUBLISHED
28 April 2025



PAPER

# Absorbed and effective dose estimates in HR-pQCT of the distal radius and tibia: virtual dosimetry with a GPU-accelerated Monte Carlo code

**Laura Antonia Cerbone**[1,2,3], **Giovanni Mettivier**[2,3,*], **Youfang Lai**[4], **Xun Jia**[4], **Steven K Boyd**[5] and **Paolo Russo**[2,3]

[1] Scuola Superiore Meridionale, I-80138 Naples, Italy
[2] Dipartimento di Fisica 'Ettore Pancini', Università di Napoli Federico II, I-80126 Naples, Italy
[3] Istituto Nazionale di Fisica Nucleare (INFN), Sezione di Napoli, I-80126 Naples, Italy
[4] Department of Radiation Oncology and Molecular Radiation Sciences, Johns Hopkins University, Baltimore, MD 21224, United States of America
[5] McCaig Institute for Bone and Joint Health, Department of Radiology, Cumming School of Medicine, University of Calgary, Calgary, Alberta T2N 4Z6, Canada
[*] Author to whom any correspondence should be addressed.

**E-mail:** mettivier@na.infn.it

**Keywords:** HR-pQCT, dosimetry, GPU, Monte Carlo simulation, virtual dosimetry trial, personalized dosimetry

Supplementary material for this article is available online

## Abstract

*Objective*. To obtain maps of absorbed dose and an estimate of the effective dose to an adult patient for a high resolution peripheral quantitative computed tomography (HR-pQCT) (XtremeCT II) examination of the distal tibia and radius, using a graphical processing unit (GPU)-based Monte Carlo (MC) code. *Approach*. We adapted the validated code gCTD (GPU-based CT Dose calculator), to replicate the HR-pQCT configuration. MC simulations were performed on digital phantoms of the tibia and radius obtained from bilateral scans of the ankle and wrist of a 25 year-old female volunteer. Scans were segmented using an ad hoc algorithm in Fiji. Simulations run on an NVIDIA GeForce RTX 3090 GPU board. MC dose estimates were validated via computed tomography dose index measurements. *Main Results*. We obtained the absorbed dose distribution in the skin, bone, bone marrow, fat, and muscle tissues. The effective dose for the HR-pQCT examination were 2.05 $\mu$Sv and 2.13 $\mu$Sv for the right and left tibia, and 1.48 $\mu$Sv and 1.49 $\mu$Sv for the right and left radius, respectively, with a Type A statistical uncertainty of 0.06% ($k = 3$) with $4.66 \times 10^{11}$ photon histories. Corresponding effective dose conversion coefficients (*k-factors*) were 0.185 $\mu\text{Sv} \cdot \text{mGy}^{-1} \cdot \text{cm}^{-1}$ (tibia), and 0.133 $\mu\text{Sv mGy}^{-1} \cdot \text{cm}^{-1}$ (radius). *Significance*. We reported the first independent estimate of the effective dose for standard HR-pQCT clinical scans of the distal tibia and radius with the XtremeCT II scanner. Effective dose estimates (considering a total relative uncertainty of less than 40%) were lower than those indicated by the manufacturer and commonly reported for these scans. With $4.66 \times 10^9$ photon histories, the gCTD MC code can produce 3D dose maps from segmented HR-pQCT images in less than 12 s (GPU time), with 0.9% ($k = 3$) statistical uncertainty, making real-time personalized dose estimate feasible.

## 1. Introduction

High-resolution peripheral quantitative computed tomography (HR-pQCT) is a tomographic imaging technique employing x-rays for studying the microarchitecture of the epiphysis of long bones (distal tibia and radius, primarily) with an *in vivo*, non-invasive technique (Boutroy *et al* 2005, Whittier *et al* 2020). It provides a quantitative assessment of the bone structure, giving both morphological and functional information on the bone strength, obtained via finite element analysis (Manske *et al* 2015, Whittier

**Table 1.** Effective doses for DXA, QCT and CBCT examinations for adults and children in different anatomical sites.

| Examination | Effective dose ($\mu$Sv) | Source |
|---|---|---|
| Adult spine DXA | 13 | Damilakis *et al* (2010) |
| Adult hip DXA | 9 | |
| Adult lumbar spine DXA (fast array mode) | 2.2 | Thomas *et al* (2005) |
| 1 year-old lumbar spine DXA (fast array mode) | 4.7 | |
| Adult forearm DXA | 0.03 | |
| 1 year-old forearm DXA | 0.14 | |
| 3D MDQCT (Mineral Density QCT) spine L1-L2 (120 kV, 100 mAs) | 1500 | Damilakis *et al* (2010) |
| 3D MDQCT hip (120 kV, 150–200 mAs) | 2500–3000 | |
| 3D MDQCT radius (120 kV, 100 mAs) | $<$10 | |
| CBCT hand-wrist standard protocol (Adult) | 1.4 | Ludlow *et al* (2018) |
| CBCT hand-wrist standard protocol (5 year-old) | 4.4 | |
| CBCT foot-ankle standard protocol (Adult) | 3.7 | |
| CBCT foot-ankle standard protocol (5 year-old) | 21.6 | |

*et al* 2020). Although HR-pQCT can be used for bone densitometry—as its outputs include volumetric bone mineral density (BMD) and compartment-specific BMD (trabecular and cortical)—it is still considered primarily a research tool (Gazzotti *et al* 2023); indeed, dual-energy x-ray absorptiometry (DXA) (Bazzocchi *et al* 2016) represents the gold standard for clinical practice (El Maghraoui and Roux 2008) and it is the accepted method to diagnose osteoporosis (World Health Organization 2004, Blake and Fogelman 2007).

HR-pQCT (XtremeCT II scanner produced by Scanco Medical AG, specifically) has also been adopted at the McCaig Institute for Bone and Joint Health (Calgary, Canada) for the assessment of bone health in astronauts before and after their spaceflight on the International Space Station (Gabel *et al* 2022a, 2022b, Kemp *et al* 2023). In parallel, a research project has recently started at the Scuola Superiore Meridionale and the Università di Napoli Federico II (Naples, Italy) for the design of a photon counting HR-pQCT compact device, dedicated to the tibia and radius, aiming to study the bone loss phenomenon in astronauts with scans performed during space missions.

Since DXA has been extensively used since the mid-80s, several dosimetry studies have been performed, with the radiation dose to the patient being well-known for both adults (Damilakis *et al* 2010, Bandirali *et al* 2013) and children (Thomas *et al* 2005). This is also true for quantitative computed tomography (QCT), which is considered an established clinical technique for measuring volumetric BMD and monitoring BMD changes with age or in response to treatment (Adams 2009, Link and Lang 2014). Radiation effective doses for DXA and QCT are reported in table 1, from which one can notice that DXA is a low radiation dose exam (0.03–13 $\mu$Sv) compared to QCT, for which the effective dose is in the order of the mSv.

Among the x-ray techniques for bone densitometry, HR-pQCT is the most recent one and represents a significant technological improvement, in terms of image resolution and the ability to resolve the internal microstructure of spongy bones. However, there is a shortage of dosimetry studies for this technique, and few independent estimates of the effective dose in HR-pQCT can be found in the literature (Burrows *et al* 2010, Quintiens *et al* 2024). Burrows *et al* (2010) reported an independent evaluation of the effective dose of less than 3 $\mu$Sv for a tibial scan in adolescents using the first-generation XtremeCT I HR-pQCT scanner (scan length 9.02 mm, tube voltage 60 kVp, tube current 900 $\mu$A, scan time 2.8 min, 100 ms integration time per projection), but they did not provide any details on the calculation. We believe that the effective dose of 3−5 $\mu$Sv, usually reported in the literature (Boutroy *et al* 2005, Krug *et al* 2010, Nishiyama and Shane 2013, Whittier *et al* 2020, Van den Bergh *et al* 2021) for HR-pQCT examinations of the tibia and radius, refers simply to the value provided by the manufacturer (effective dose below 5 $\mu$Sv using the XtremeCT II with a scan length 10.8 mm, 68 kVp tube voltage, 1470 $\mu$A tube current, 2 min scan time, 43 ms integration time per projection) (Scanco Medical 2015).

This work aims (*i*) to investigate the patient-specific 3D-distribution of absorbed dose in the exposed tissues of the distal tibia and radius, and (*ii*) to provide a first estimate of the personalized effective dose for clinical scans with the XtremeCT II unit. To this end, we developed a graphical processing unit (GPU)-accelerated, Monte Carlo (MC)-based simulation platform for a virtual HR-pQCT scan, providing a detailed description of the procedure to compute the corresponding effective dose. We set up a platform (virtual imaging trial for osteoporosis, VIT-OSTEO) for virtual imaging and dosimetry for HR-pQCT and DXA scans, validated via computed tomography (CT) dose measurements, by developing *ad hoc* digital twins of the scanners and anthropomorphic digital phantoms derived from actual HR-pQCT scans of the

**Table 2.** Scan parameters used for a 'standard protocol' for the tibia and radius with the Scanco Medical XtremeCT II scanner.

| Scan parameters | Tibia and radius standard protocol |
|---|---|
| Num. of rotations | 1 |
| Focal spot dimension ($mm^2$) | $0.06 \times 0.06$ |
| Tube voltage (kVp) | 68 |
| Tube current (mA) | 1.47 |
| Time current product (mAs) | 71 |
| Integration time (ms) | 43 |
| Measure time (min) | 2 |
| Number of projections/angle | 900/180° |
| Total scan angle, total number of projections | 202°, 1011 |
| Scan length ($L$) in the axial direction (mm) | 10.2 |
| Voxel dimension ($\mu m^3$) | $60.7 \times 60.7 \times 60.7$ |
| Number of reconstructed slices | 168 |
| Image matrix dimension (pixel) | $2304 \times 2304$ |
| Scan field of view (FOV) diameter (mm) | 140 |
| Source to isocenter distance (cm) | 40 |
| Source to detector distance (cm) | 60 |

distal tibia and radius in an adult patient. This work presents the VIT-OSTEO tool for HR-pQCT, while a future work will present the DXA tool of the VIT-OSTEO platform.

Virtual trials are emerging as an invaluable tool for innovations in medical imaging (Abadi *et al* 2024). In this framework, MC-based dosimetry in diagnostic radiology—using mathematical phantoms representing the patient anatomy (Boone *et al* 2017)—can be used to examine the dose deposition in detail, as well as to estimate the organ dose, from which the effective dose can be estimated. By accurately reproducing the x-ray spectrum and the geometry of such examinations in a virtual dosimetry study, using realistic computational phantoms, it is possible to perform dosimetry studies for radiographic techniques, including planar radiography, mammography, breast CT, and CT examinations (Kim *et al* 2011, Yi *et al* 2011, Jia *et al* 2012a, di Franco *et al* 2020, Mettivier *et al* 2024). This work intends to add HR-pQCT to the various diagnostic imaging modalities for which MC-based virtual dosimetry is available.

## 2. Materials and methods

### 2.1. Original data

The CT images used in this study were acquired using an HR-pQCT scanner (XtremeCT II, Scanco Medical AG, Brütisellen, Switzerland). Bilateral tibia and radius scans of a 25-year-old female volunteer (176.6 cm body height, 78.3 kg body mass, body mass index (BMI) 25.1, areal BMD (aBMD) L1–L3 1.19 $g \cdot cm^{-2}$) were obtained following the standard tibia protocol (Whittier *et al* 2020). Scanner parameters used to acquire images are listed in table 2. The original files were imported into the image processing freeware Fiji (Schindelin *et al* 2012) as raw 16-bit signed files. Images were calibrated using the following linear function (provided by the manufacturer) to quantitatively assess bone density, expressed in milligrams of hydroxyapatite for cubic cm (mg HA $\cdot$ $cm^{-3}$):

$$P_{\text{den}} = P \cdot 0.19701564 - 392.247 \tag{1}$$

where $P$ represents the pixel value in the original image, expressed as a value between 0 and 65 535 (16-bit). Pixel values ($P_{\text{den}}$) in the calibrated images express the density in mg HA $\cdot$ $cm^{-3}$; for the images reported in figure 1 the values ranged from $-800$ mg HA $\cdot$ $cm^{-3}$ to $+1600$ mg HA $\cdot$ $cm^{-3}$, with the highest values corresponding to cortical bone.

The calibration scale in mg HA$\cdot$ $cm^{-3}$ has a physical meaning for bone tissue only, while the used calibration function produces non-physical negative values for air and soft tissues. Figures 1(c) and (d) show the histograms of calibrated pixel values with the de-convolved three Gaussian peaks associated to the three materials (air, soft tissue and bone). Thresholds for tissue segmentation (see section 2.3) were selected around the valley between peaks 1 and 2 for the soft tissue (lowest bone density), and peaks 2 and 3 for the bone (highest bone density).

### 2.2. Scanner characterization: CTDI and DLP measurements

We measured the CT dose index in air ($CTDI_{100-\text{in}-\text{air}}$) for the HR-pQCT scanner used to acquire the CT images used in this study. The measurement was performed using a 100 mm ionization chamber (Radcal

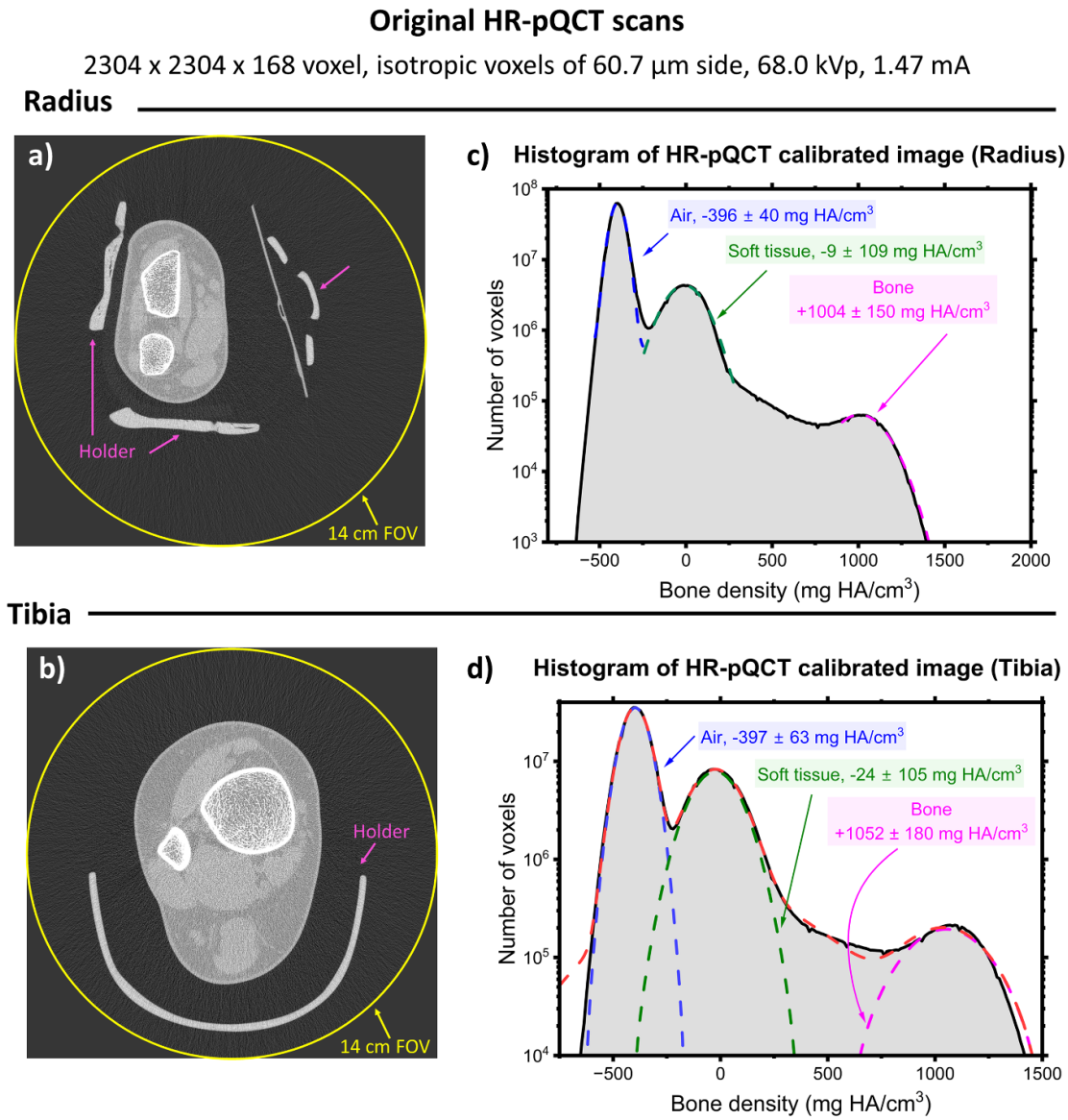


**Figure 1.** Original HR-pQCT image (central slice) of a radius (a) and a tibia (b) acquired with the XtremeCT II scanner (Scanco Medical). Corresponding histograms of the calibrated images (pixel value expressed in units of mg HA $cm^{-3}$) are reported (c), (d). Histograms show three peaks associated with the air, soft tissue, and bone tissue voxels contained within the field of view, fitted as the sum of three Gaussian distributions (dashed lines), of which means and standard deviations are indicated. Please note that the calibration has a physical meaning only for bone tissue voxels. When applying the calibration for the whole picture, negative values arise for air and soft tissue voxels.

10X6-3CT) connected to an Accu-Gold+ Touch Radcal dosimeter (Radcal, Monrovia, CA, USA). The chamber was positioned at the center of the device's field of view, supported by a paper stand. We used a scout view to locate the center of the chamber's sensitive volume, around which a standard scan was performed (68 kVp, 1.47 mA, 71 mAs). The measured value for $CTDI_{100-in-air}$ was 12.81 mGy ± 4%. In addition, we measured the dose length product (DLP), $DLP = CTDI_{vol} \cdot L$, where $CTDI_{vol}$ is the volume CT dose index (measured value 10.98 mGy, value reported on the scanner console 10.8 mGy) and $L$ is the scan length (1.02 cm). To this end, we used a CTDI pediatric head cylindrical phantom (PMMA, 100 mm diameter) and the same dosimeter used for the $CTDI_{100-in-air}$ measurement. The corresponding value was $DLP = 11.2$ mGy · cm ± 4%, showing a deviation of 1.8% from the value reported on the scanner console (11.0 mGy · cm).

### 2.3. Phantom segmentation

HR-pQCT images of the tibia were segmented using an algorithm in Fiji (figure 2). An in-depth description of the segmentation procedure is given in the Supplementary material, together with the information on material elemental composition and density (table S1).

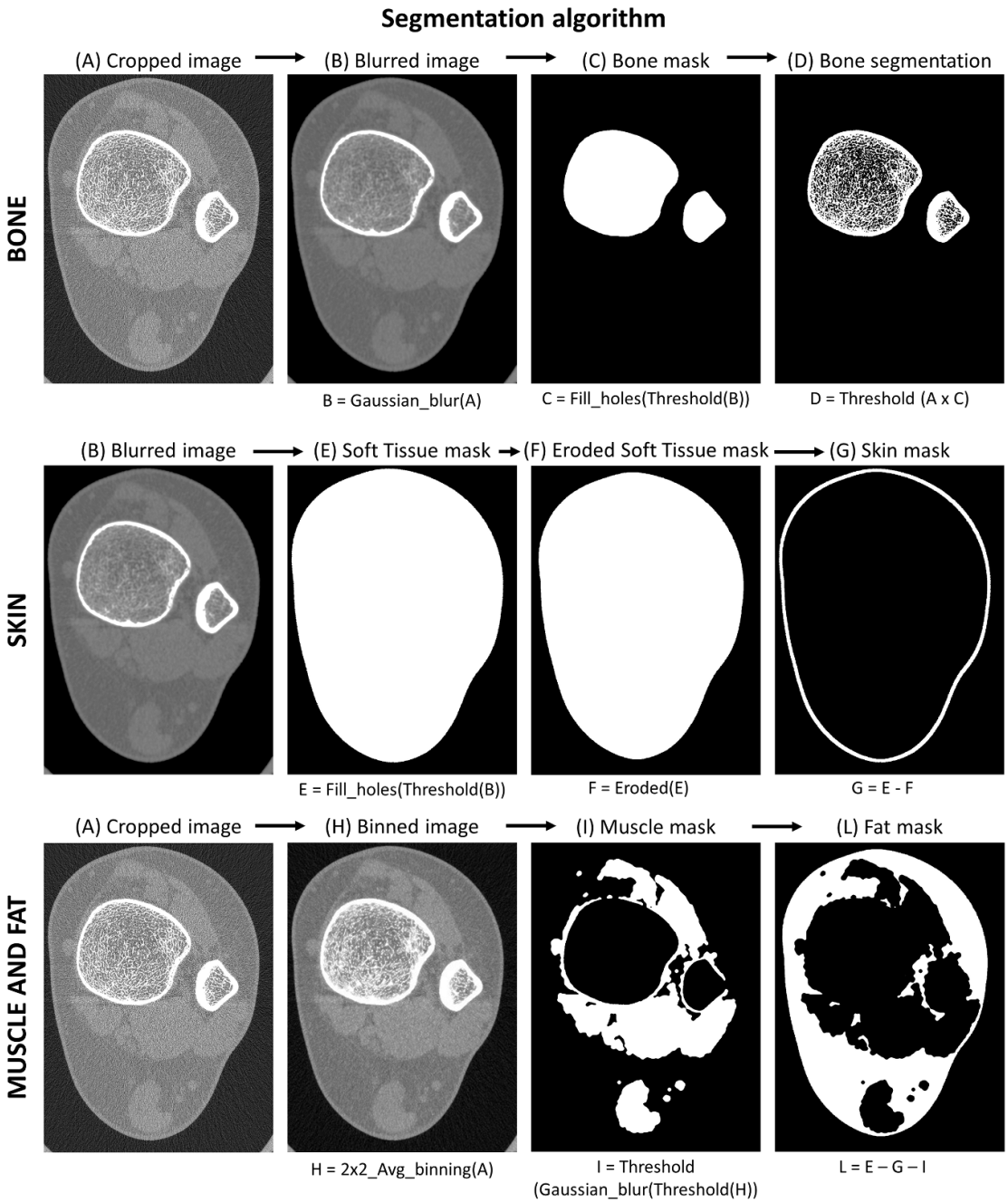


**Figure 2.** Showing the steps of the segmentation algorithm (performed with the Fiji software) to isolate separately the bone, skin, muscle, and adipose tissues within the HR-pQCT image of the tibia.

The segmentation of the bone was performed by first identifying the bone contour (figure 2(C)) —applying a lower threshold of 200 mg HA · $cm^{-3}$—and then isolating the trabecular bone contained within the contour using a lower threshold of 70 mg HA · $cm^{-3}$ (figure 2(D)). Please note that we created a single mask for bone, including both the trabecular and cortical bone, which were assumed to have the same density and elemental composition (see Supplementary material, table S1). While the two tissues may be apparently different in CT imaging due to partial volume effect (Ito *et al* 2005), our assumption is reasonable as trabecular and cortical bone have the same density, differing by 3% at most (Gong *et al* 1964).

The thresholds we used differ from those recommended in the HR-pQCT guidelines (Whittier *et al* 2020), where thresholds of 450 mg HA · $cm^{-3}$ and 320 mg HA · $cm^{-3}$ are used for cortical bone and trabecular bone, respectively. However, for our digital phantoms, we observed that using this threshold (320 mg HA · $cm^{-3}$) resulted in a significant loss of segmented trabecular bone volume—approximately 50% of the volume obtained with the lower threshold of 70 mg HA · $cm^{-3}$. Therefore, we opted to retain the lower threshold (70 mg HA · $cm^{-3}$) in the final segmentation algorithm for the tibia and radius. However, to study the influence of such threshold choice on the final dose estimate, we repeated the segmentation

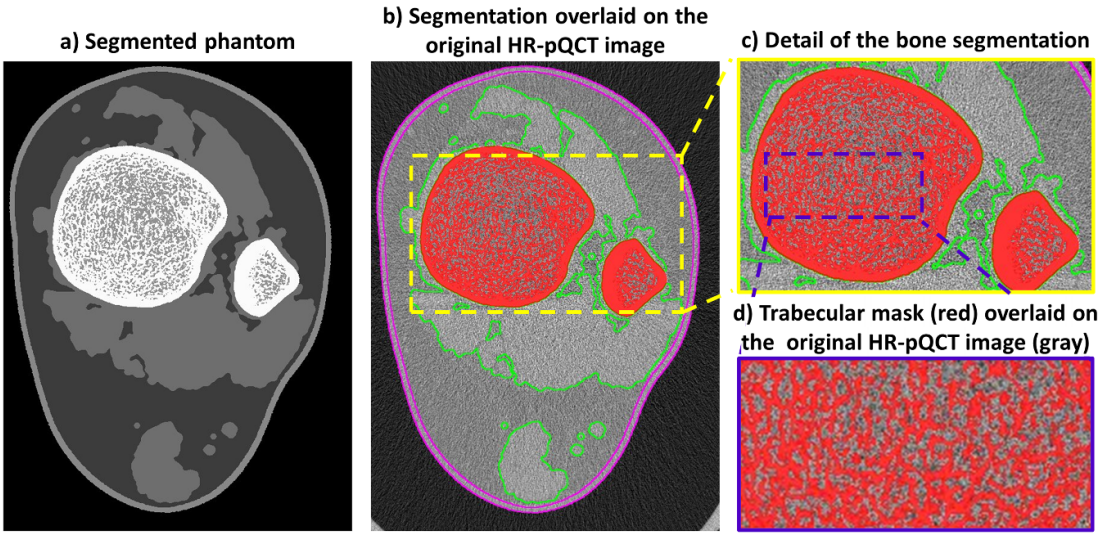


**Figure 3.** (a) The segmented phantom with different pixel values assigned to the skin, fat, and muscle and bone (cortical and trabecular bone were modeled as being the same material). The quality of the segmentation can be assessed visually by observing the overlay of the segmented tissues over the original HR-pQCT image (b). Panel (c) shows the detail of the bone segmentation; panel (d) shows a closer look at the mask,in red, overlaid on the original HR-pQCT image to visually evaluate the quality of the segmentation in the most internal part of the bone. Color legend: red = bone; green = muscle; purple = skin; remaining tissue = fat.

procedure using the recommended thresholds for one of the four anatomical sites (left tibia). Then, we repeated the simulation for the two phantoms and analyzed the resulting effective doses (section 2.9).

The segmentation resulting from our algorithm was compared visually with the original HR-pQCT image by overlaying the two images (figure 3(b)), showing good visual correspondence between anatomical compartments in the original CT and the segmented areas. The digital phantoms created for this work have a voxel size as small as 120 $\mu$m × 120 $\mu$m × 120 $\mu$m. This allows to keep the spatial resolution close to the original resolution of the HR-pQCT images (60.7 $\mu$m voxel side) from which they were obtained, as well as to determine with sufficient accuracy the dose to the surface of the bone—the endosteum—and to the bone marrow contained within medullary cavities (both relevant to the determination of the effective dose for our HR-pQCT examinations, see section 2.9).

### 2.4. GPU-accelerated MC code

The MC code used in this work is based on the code called gCTD (GPU-based CT Dose calculator) (Jia *et al* 2012a, 2012b), a GPU-based MC code built using the CUDA programming environment, developed in 2011 by the team of the University of Texas Southwestern Medical Center. In this code, the Woodcock tracking method (Woodcock *et al* 1965) is employed to model photon transport, accounting for Compton scattering, Rayleigh scattering, and photoelectric absorption. Photons continue to propagate until their energy drops to 1 keV or they exit the phantom. The cross-sections for the three interactions are sourced from a subroutine (material.f) of the PENELOPE MC simulation code (Sempau *et al* 1997) and restructured using an in-house code to suit the input format of gCTD. Additionally, form factors for Compton and Rayleigh scattering are generated from PENELOPE. Energy deposition is recorded at the sites of inelastic interactions. Secondary electrons are assumed to deposit their energy locally, as their range is typically small in the keV energy range. For example, the CSDA (continuous slowing down approximation) range for a 50 keV electron in water is 43 $\mu$m, i.e. less than the pixel size (120 $\mu$m) (Berger *et al* 2005). The MC code was run on a DELL Alienware Aurora R11 desktop computer (Intel i9-10900KF, 3.70 GHz, 128 GB DDR4 RAM 3200 MHz) equipped with an NVIDIA GeForce RTX 3090 GPU memory featuring a 1.70 GHz boost clock, 10 496 CUDA cores, and 24 GB of dedicated GDDR6X memory. The software simulates a cone-beam CT exam adopting an anthropomorphic segmented phantom. The output of the MC simulation includes the CT projections and the voxel-wise absorbed dose map in the phantom (figure 5). The absorbed dose in each voxel is calculated by dividing the total energy (in eV) deposited by photons in a voxel by the voxel's mass (in grams), and then converting this value to J·kg$^{-1}$ or Gray (Gy). The MC software allows for simulating either an energy integrating detector or a spectral photon counting detector. In this last case, the user can select the energy thresholds for sorting the photons impinging on the detector in different energy bins. The MC software therefore allows for both dosimetry study and image quality assessment. In this work, we focused on dose

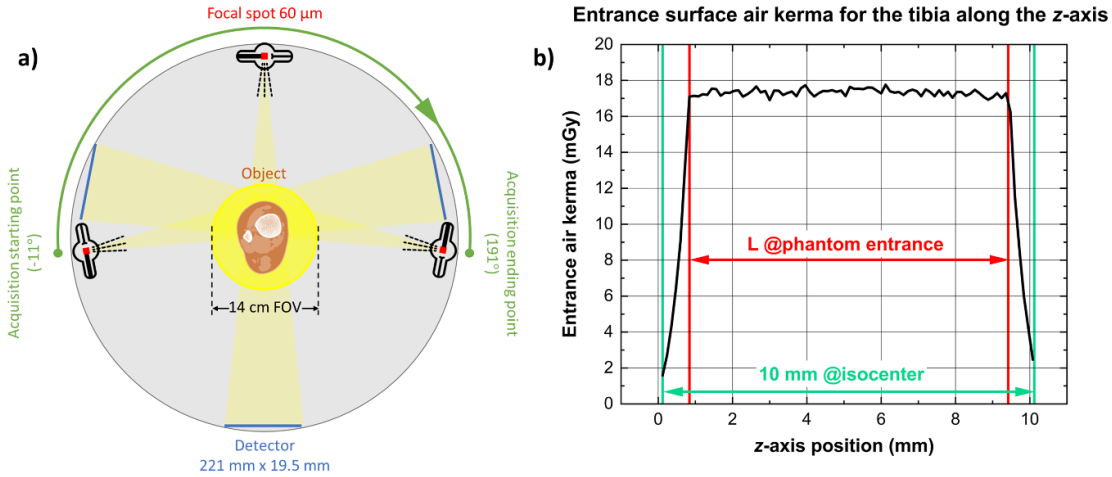


**Figure 4.** (a) A scheme of the simulated CT scanner geometry. (b) The axial profile of the entrance surface air kerma: this plot shows that, with a scan length of $L = 10$ mm set at the isocenter, the scanning length is smaller at the entrance surface due to the x-ray beam cone angle in the $z$-axis.

maps produced by the MC software, which contain the dose to medium—expressed in $\mu$Gy—absorbed in the phantom, for each projection. The voxel-wise map of the absorbed dose in the phantom for the CT exam can be obtained by summing single-view maps produced at every projection angle.

### 2.5. Scanner simulation

The MC code simulates a cone beam CT scanner with a fan beam full aperture of 22° and an axial collimation of 10 mm at the scanner isocenter, acquiring 1011 projections over a scan angle of 202°, with the scan starting from a fixed angle (figure 4(a)). Since the scan length is set to be 10 mm at the isocenter, the width of the beam in the axial direction ($z$) at the entrance of the phantom will be smaller. As a consequence, the first and last slices of our digital phantoms (whose thickness is 10.08 mm) will not be fully within the x-ray beam (figure 4(b)). The x-ray focal spot was simulated as a 0.06 mm-side square uniform source. The x-ray spectrum used by the HR-pQCT scanner is a 68 kVp spectrum with an inherent filtration of 1 mm Al and 0.2 mm Cu and an additional filtration of 0.3 mm of Be given by the tube window (half value layer, HVL, 4.5 mm Al) (Scanco Medical 2015). This spectrum was reproduced using the software SpekPy (Poludniowski *et al* 2021) accessed on the web (https://spekpy.smile.ki.se) and inserted in the MC code. MC validation is reported in the Supplementary material.

### 2.6. MC dose calibration

We calibrated the number of photon histories per projection launched in the MC simulation such that the simulated $CTDI_{100\text{-in-air}}$ matched the one measured for an actual HR-pQCT scan performed with the XtremeCT II (section 2.2). We simulated a 15 cm × 15 cm × 15 cm air phantom with 0.5 mm cubic voxel placed at the scanner isocenter. We simulated a 1011-projection scan, with $4.61 \times 10^8$ photons launched for each projection, i.e. a total of $4.66 \times 10^{11}$ primary photons ($4.61 \times 10^8$ photons/projection × 1011 projections) launched for a CT scan. To replicate the ionization chamber measurement, we generated the pixel-wise absorbed dose map, and measured the average absorbed dose, within a 6 $cm^3$ air volume. This value was scaled by the scan length and compared to the measured value. From the simulations, the $CTDI_{100\text{-in-air}}$ was calculated as 12.771 97 ± 0.0024 mGy, where the reported uncertainty is the $3\sigma$ statistical uncertainty of the MC simulations (see section 2.7).

### 2.7. MC statistical uncertainty

To assess the statistical uncertainty of the MC simulations, we repeated ten times the simulation used for the dose calibration (batch method, Walters *et al* 2002). For each simulation (for a total of $4.66 \times 10^{11}$ primary photons launched in each virtual scan), we computed the $CTDI_{100-\text{in}-\text{air}}$ and derived the mean value and the standard deviation of the mean of the ten repetitions. The corresponding relative uncertainty was $\sigma = 0.02\%$ (standard deviation of the mean divided by the mean of the ten repetitions). We therefore considered an uncertainty of $3\sigma$ ($k = 3$) on average absorbed dose derived via dose maps (section 2.8).

### 2.8. Absorbed dose computation via dose maps

We simulated HR-pQCT scans of the left and right tibia and radius from the same patient, and we obtained the 3D dose maps for the four limbs. The absorbed dose distribution in individual tissues (skin, adipose, muscular, and bone tissue) was derived from the total dose map by using the tissue masks previously obtained via segmentation. From the tissue dose maps, the mean value $\left(\overline{D_{\mathrm{T}}}\right)$ and the standard deviation (SD) of the absorbed dose in the tissue $T$ were obtained as follows:

$$\overline{D_{\mathrm{T}}} = \frac{\sum_{ijk}\delta_{\mathrm{T},ijk}\cdot m_{ijk}\cdot D_{ijk}}{\sum_{ijk}\delta_{T,ijk}\cdot m_{ijk}} \tag{2}$$

$$\mathrm{SD} = \sqrt{\frac{1}{N_{\mathrm{T}}-1}\sum_{i,j,k}^{N_{\mathrm{T}}}\left(D_{\mathrm{T}}^{ijk}-\overline{D_{\mathrm{T}}}\right)^2} \tag{3}$$

where $N_{\mathrm{T}}$ is the number of voxels of tissue $T$ contained in the phantom, $(i,j,k)$ are the voxel coordinates in the phantom in the $x$, $y$, and $z$ directions, respectively, with $k$ corresponding to the slice number, $m_{ijk}$ and $D_{ijk}$ are the mass and absorbed dose of voxel $(i,j,k)$, respectively, and $\delta_{\mathrm{T},ijk}$ is 1 if voxel $(i,j,k)$ belongs to organ or tissue T and 0 otherwise. The standard deviation SD here indicates the spread of the absorbed dose distribution in each tissue and can therefore be viewed as a measure of the homogeneity of the dose map for that tissue. Specifically, we defined a homogeneity index HI using equation (4). Hence, HI equal to zero corresponds to a completely uniform dose distribution,

$$\mathrm{HI} = \mathrm{SD}/\overline{D_{\mathrm{T}}}. \tag{4}$$

Since in the case of the skin and the bone, the relevant tissue for the computation of the effective dose is not the entire tissue volume, but its surface, we computed the average absorbed dose in the surface of the skin and the bone (see Supplementary material). For the absorbed dose in the bone endosteum, we observe that our simulations did not consider the dose enhancement that occurs in the endosteal region of the trabeculae. Indeed, in bone dosimetry, current methods for estimating the absorbed dose include the calculation of bone tissue dose response function and dose enhancement factors (International Commission on Radiological Protection (ICRP) 116, Lee *et al* 2006, Johnson *et al* 2011). Such factors need to be considered for photon energy below 200 keV. Photons in this energy range absorbed in the bone marrow contained in the medullary cavities produce, indeed, secondary particles which deposit their energy in the adjacent endosteum of trabeculae (in the order of 10 $\mu$m thickness of bone), leading to local dose enhancement (Zankl *et al* 2021). However, in our gCTD MC code, electrons deposit their energy locally (in the voxel in which they are produced) and they are not tracked in the tissues.

As previously stated, for the effective dose computation performed in this work (section 2.9 below), we used the average absorbed dose in the bone surface. However, for comparison, we also calculated the endosteum absorbed dose following the approach of ICRP 116 Annex D (ICRP 2010), by considering the reported factors for bone-specific absorbed dose to endosteum per photon fluence (figure 2(d), Annex D, ICRP 116) multiplied by the maximum photon fluence incident on the bone surface in our scans.

### 2.9. Effective dose computation

The effective dose, $E$, is defined by the ICRP in the ICRP 103 report as a radioprotection quantity used for comparing relative doses from different diagnostic procedures. From the estimated $E$ value for a diagnostic exam, one can calculate the possible risk of radio-induced patient detriment (ICRP 2007). Effective dose estimates for partial irradiation of the body volume can be computed from the average absorbed dose $\overline{D_{\mathrm{T}}}$ using the following formula:

$$E = w_{\mathrm{R}}\cdot\sum_{\mathrm{T}} w_{\mathrm{T}}\cdot\left(f_{\mathrm{T}}\cdot\overline{D_{\mathrm{T}}}\right) \tag{5}$$

where $w_{\mathrm{R}}$ is the radiation weighting factor, which accounts for the type of radiation; $f_{\mathrm{T}}$ is the fraction of tissue $T$ irradiated during the procedure; $\overline{D_{\mathrm{T}}}$ is the mean absorbed dose in the tissue $T$, and $w_{\mathrm{T}}$ is the tissue weighting factor (ICRP 2007). For x-ray photons, the radiation weighting factor $w_{\mathrm{R}}$ in equation (5) equals 1. The number and type of tissues included in this computation depend on the anatomical region being examined.

Following the method for computing effective doses for a CBCT examination of the ankle adopted by Koivisto *et al* (2015), we included bone surface, skin, bone marrow, and muscle. Irradiated fraction of the tissues considered in the effective dose computation, and thecorresponding weighting factors, are listed in tables 3 and table 5, respectively. A detailed description of the calculation of irradiated organ fractions can be

**Table 3.** Irradiated fractions ($f_T$) of radiosensitive organs. For the muscle, fat, and yellow bone marrow (YBM) total tissue refers to the total mass of tissue contained in the body of a reference female adult (ICRP 2002). For bone and skin, the total tissue refers to the total surface of the skeleton (including trabecular and cortical bone) and the total surface of the skin, respectively. Tissue densities are reported in $g \cdot cm^{-3}$.

| TIBIA | | | | | |
|---|---|---|---|---|---|
| | Tissue in the phantom (surface or mass) | | Total tissue (surface or mass) | Irradiated fraction $f_T$ | |
| Tissue type (density) | Right tibia | Left tibia | | Right tibia | Left tibia |
| Bone surface ($1.85\ g \cdot cm^{-3}$) | 148.7 $cm^2$ (11.7 g) | 144.5 $cm^2$ (11.3 g) | $1.48 \times 10^5$ $cm^2$ | 0.0010 | 0.0010 |
| Skin surface ($1.10\ g \cdot cm^{-3}$) | 26.5 $cm^2$ (3.2 g) | 26.7 $cm^2$ (3.2 g) | $1.94 \times 10^4$ $cm^2$ | 0.0014 | 0.0014 |
| Muscle ($1.05\ g \cdot cm^{-3}$) | 15.6 g | 16.2 g | 17 500 g | 0.0009 | 0.0009 |
| Fat ($0.99\ g \cdot cm^{-3}$) | 19.2 g | 17.8 g | 18 000 g | 0.0011 | 0.0010 |
| YBM ($1.03\ g \cdot cm^{-3}$) | 2.7 g | 2.7 g | 1800 g | 0.0015 | 0.0015 |
| Total weight | 52.3 g | 51.3 g | | | |
| RADIUS | | | | | |
| | Tissue in the phantom (surface or mass) | | Total tissue (surface or mass) | Irradiated fraction $f_T$ | |
| Tissue type (density) | Right radius | Left radius | | Right radius | Left radius |
| Bone surface ($1.85\ g \cdot cm^{-3}$) | 84.9 $cm^2$ (5.0 g) | 89.2 $cm^2$ (5.3 g) | $1.48 \times 10^5$ $cm^2$ | 0.0006 | 0.0006 |
| Skin surface ($1.10\ g \cdot cm^{-3}$) | 17.5 $cm^2$ (2.1 g) | 17.5 $cm^2$ (2.1 g) | $1.94 \times 10^4$ $cm^2$ | 0.0009 | 0.0009 |
| Muscle ($1.05\ g \cdot cm^{-3}$) | 7.5 g | 7.6 g | 17 500 g | 0.0004 | 0.0004 |
| Fat ($0.99\ g \cdot cm^{-3}$) | 6.6 g | 5.5 g | 18 000 g | 0.0004 | 0.0003 |
| YBM ($1.03\ g \cdot cm^{-3}$) | 1.4 g | 1.3 g | 1800 g | 0.0008 | 0.0007 |
| Total weight | 22.6 g | 21.8 g | | | |

found in the Supplementary material. To estimate the effective dose, we considered the absorbed dose to be negligible for all organs not directly exposed during the scan (see Supplementary material for a discussion of the bias introduced by this assumption).

*2.9.1. Effective dose conversion coefficients*

Dosimetry for CT examinations uses the product of the (in-phantom) volume CT dose index ($CTDI_{vol}$) and the scan length, termed DLP, as a reference value for each CT scan. From the DLP, the effective dose can be computed via MC-calculated conversion factors (*k-factors*) (Huda *et al* 2008) using the following formula:

$$k - \text{factor} = \frac{E\ (\mu\text{Sv})}{\text{DLP}\ (\text{mGy} \cdot \text{cm})}, \tag{6}$$

where $E$ is the effective dose. We calculated the ratio between the estimated effective dose and the measured DLP (see section 2.2) to obtain the *k-factors* for the tibia and radius examinations.

## 3. Results

### 3.1. Tissue absorbed dose

The presented GPU-based MC code provided voxel-wise absorbed dose maps of the digital phantoms for each projection. Figure 5 shows the central slice of a 3D dose map in the tibia, irradiated from a single projection angle (−11°, 90°, or 191°), making evident the marked dose gradient in the direction of the incident beam produced for a single projection irradiation. Also shown is the shadow effect produced on adjacent tissues by the shielding action of high-absorbing bone tissue. By summing the calculated 1011 dose maps for single projections, we obtained the 3D voxel-wise absorbed dose maps in the phantom, for the CT scan. We then derived the average absorbed doses for both the entire phantom and individual tissues (table 4). Such doses were used to compute the effective dose for an HR-pQCT examination of the tibia (figure 6) and the radius (figure 9). Please note that the relative statistical uncertainty of the MC simulations of absorbed doses were 0.06% ($k = 3$).

### 3.2. Tibia

The average absorbed dose in the tibia for an HR-pQCT examination was 9.1 mGy for the right leg, and 9.2 mGy for the left leg (table 4). The 2D distribution of the absorbed dose in the central slice of the tibia

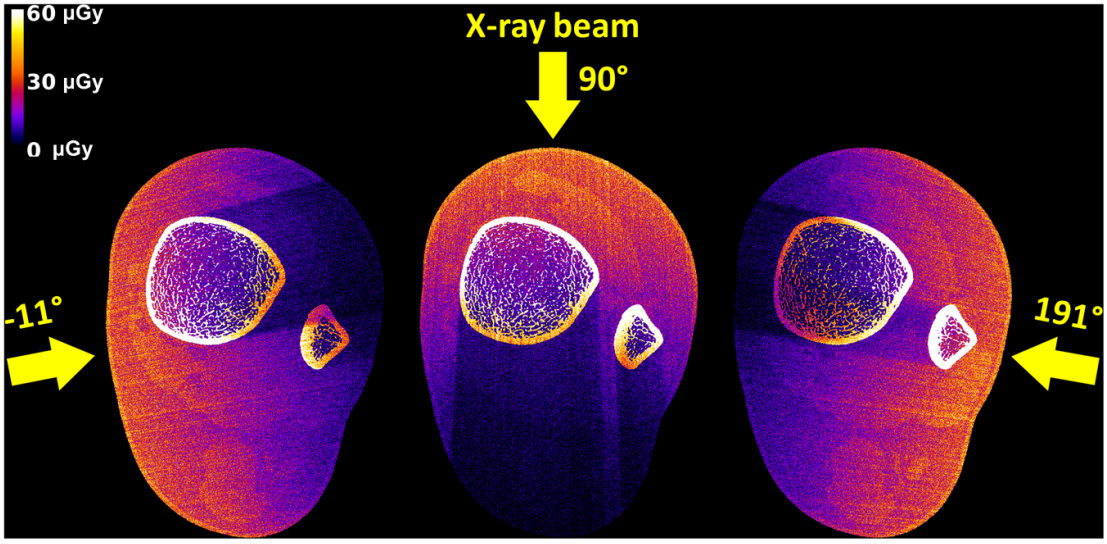


**Figure 5.** Absorbed dose maps in the central slice of the tibia for three single projections (angular position of the source −11°, 90°, or 191°). By summing the 3D dose maps for the 1011 projections, one obtains the absorbed dose maps for the whole CT scan (figure 6). Note that the scale is in $\mu$Gy units, as these dose maps are obtained from single projections.

**Table 4.** Mean absorbed dose (mGy) in the tibia and radius for the entire phantom (total) and for separate tissue components in the virtual HR-pQCR scan. The statistical uncertainty on the MC dose estimates is 0.06% ($k = 3$). For each organ dose, the value in parenthesis reports the homogeneity index HI defined by equation (4).

| | TIBIA | | RADIUS | |
|---|---|---|---|---|
| | Right tibia | Left tibia | Right Radius | Left Radius |
| Mean dose to the phantom (mGy) | 9.1 (HI = 89%) | 9.2 (HI = 91%) | 12.0 (HI = 92%) | 12.5 (HI = 93%) |
| Dose to bone (mGy) | 26.6 (38%) | 27.5 (38%) | 38.3 (26%) | 38.6 (25%) |
| Dose to bone surface (mGy) | 26.6 (39%) | 26.8 (36%) | 37.7 (25%) | 37.9 (25%) |
| Dose to skin (mGy) | 9.3 (40%) | 9.3 (39%) | 10.0 (30%) | 10.0 (29%) |
| Dose to skin surface (mGy) | 27.9 (61%) | 27.8 (60%) | 31.7 (51%) | 31.8 (50%) |
| Dose to muscle (mGy) | 6.1 (42%) | 6.(41%) | 8.2 (23%) | 8.2 (24%) |
| Dose to fat (mGy) | 6.7 (41%) | 6.8 (40%) | 7.9 (31%) | 7.9 (32%) |
| Dose to YBM (mGy) | 4.2 (28%) | 4.4 (29%) | 6.0 (23%) | 6.1 (22%) |

phantom is displayed in figure 6, where it can be noticed that, both in the air and in the phantom, the absorbed dose is higher towards one side. This effect is due to the scan being performed over a scan angle of (202°−180° + beam fan angle of 22°) (figure 4), instead of 360°, as occurs in whole-body CT clinical scans.

This is also evident in figure 7(c), which displays a line profile across the tibia dose map. An exponential fit (red line) to this profile gives a qualitative indication of the dose trend. To quantitatively assess the non-uniformity of the dose distribution, we computed the highest dose gradient across each slice (about 1.5 mGy · mm$^{-1}$), corresponding to a maximum relative dose variation of 330% along the line profile. Analyzing a line profile across the 2D dose map (figure 7(a)), one can notice that the highest absorbed dose is found within the cortical bone, with voxels reaching absorbed dose values as high as 63 mGy. Globally, the dose decreases exponentially moving towards the center of the phantom, where the trabecular tissue is shielded from surrounding tissues. The same cup-like profile is found for both the tibia (bigger bone on the left in figure 7(b)) and the fibula (smaller bone on the right in figure 7(b)). The slice-by-slice mean absorbed dose in bone can also be derived from the 3D dose map: a variation of approximately 2.5% was observed along the $z$-direction. This variation is partly due to changes in the photon flux along the axial direction (estimated to the 1% level), and partly to the anatomical variability of the ankle itself. It is important to point out that such a variation was computed on the central 74 slices, excluding the first and last 5 slices, where the geometry of irradiation caused a lower dose (cone beam geometry with a 10 mm collimation defined at isocenter, as discussed in section 2.5).

The total absorbed dose map was divided into individual tissues (figure 8), to extrapolate the mean absorbed dose values for the bone, bone marrow, muscle, fat, and skin (table 4). The skin surface (outer 60 $\mu$m thick layer of the skin) and the bone (cortical and trabecular) absorb the highest dose, with an average value of 27.9 mGy and 26.6 mGy, respectively. We also computed the absorbed dose in the bone endosteum

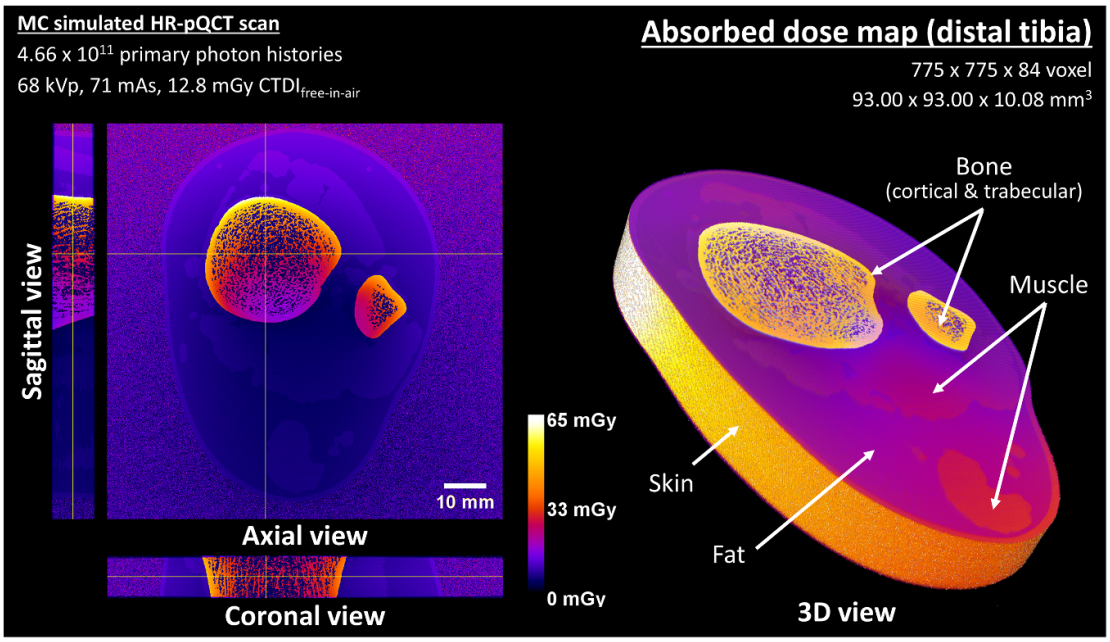


**Figure 6.** Axial, coronal, and sagittal views in the central slice of the 3D map of absorbed dose (mGy) derived from the MC simulation of a clinical HR-pQCT scan of an ankle. The voxelized tibia phantom was segmented into bone tissue, bone marrow (modeled as soft tissue), fat, muscle, and skin. Absorption by the air voxel outside the phantom was also simulated. The partial angular scan (202°) produces a higher exposure on one side of the phantom. The dose scale shown refers to the three CT views only.

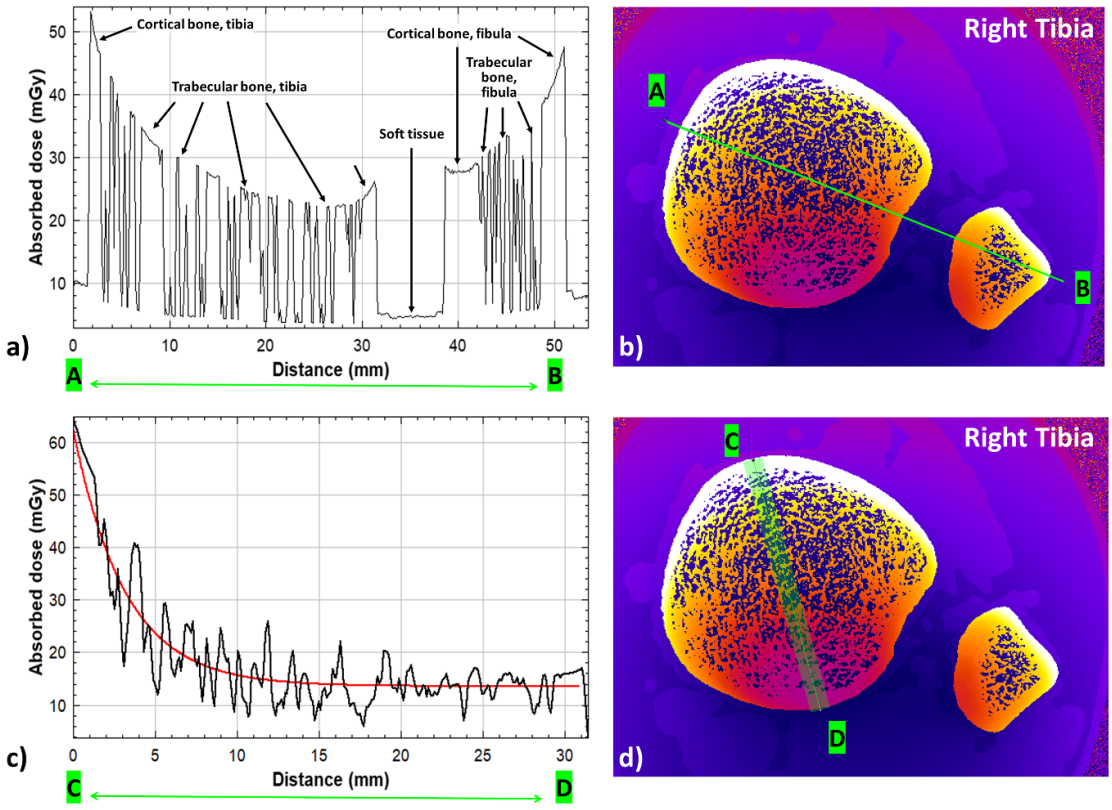


**Figure 7.** (a) Dose profile along a linear selection on the absorbed dose map of the ankle (b), crossing both the tibia and the fibula (from point A to point B). Figure (c) shows the dose profile on the tibia in the direction of the highest dose gradient (line selection is shown in Figure *d*, from point C to point D, as an average of several line profiles). The continuous red line in panel (c) shows an exponential fit to the averaged line profile.

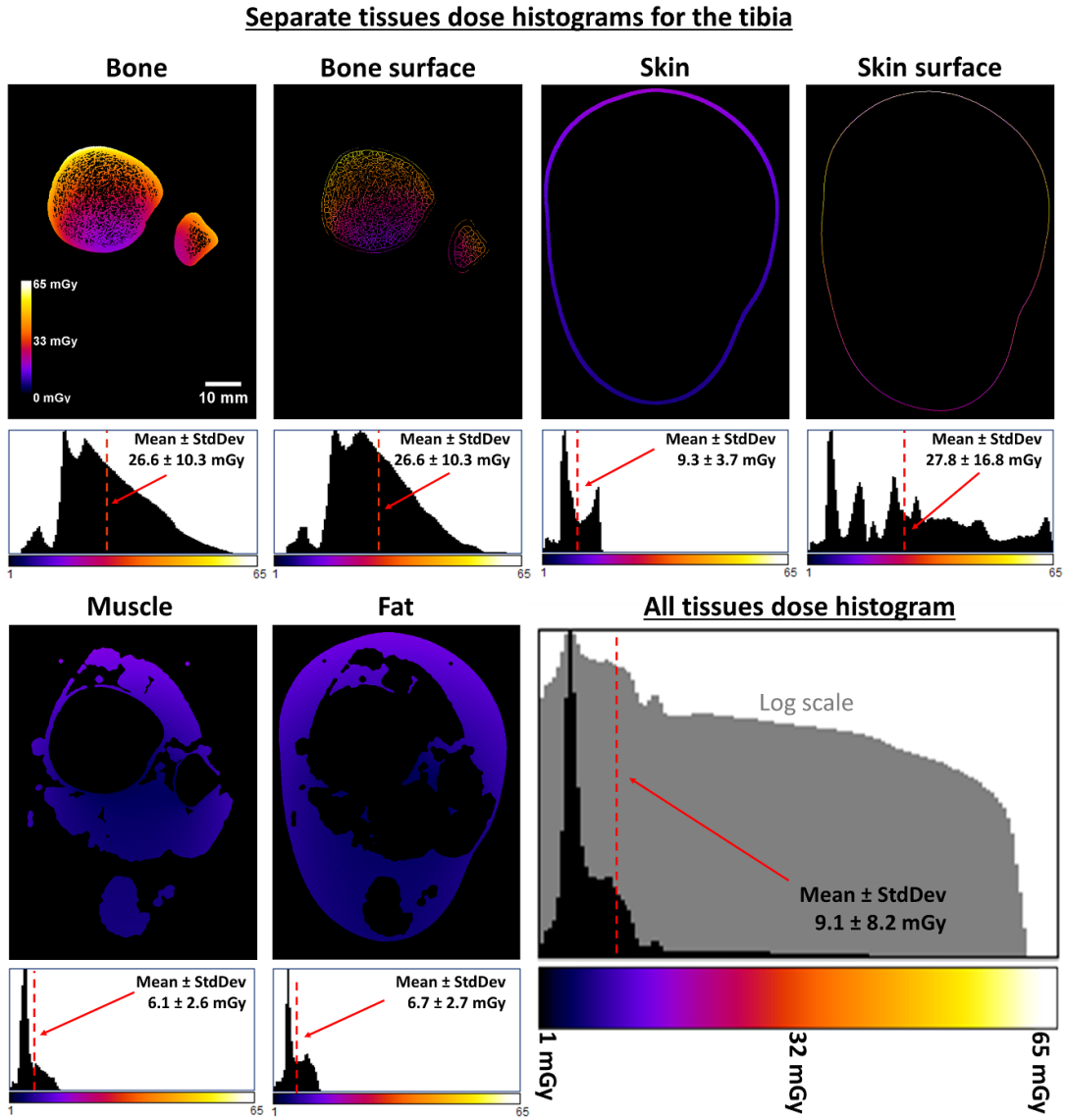


**Figure 8.** Showing absorbed dose maps (mGy) in the four separate tissues (bone, muscle, fat, and skin) of the tibia, and the corresponding histograms. The histogram of the absorbed dose in the whole phantom is also shown (excluding the air surrounding it).

using energy-dependent absorbed dose per unit fluence factors, following the ICRP 116 Annex D (ICRP 2010) (section 2.8). From figure 2(d) in ICRP 116 Annex D, we selected the factor at 40 keV (corresponding to the average energy of the 68 kVp x-ray spectrum used in our simulations), i.e. $6 \times 10^{-17}$ Gy · m$^2$. Considering a bone surface of $12.3 \times 10^{-4}$ m$^2$ for the tibia (measured from the digital phantom of the tibia) and an incident photon fluence of $4.5 \times 10^{14}$ m$^{-2}$, we estimated an average absorbed dose to the tibia endosteum of 27 mGy.

### 3.3. Radius

The average absorbed dose in the radius is 12.0 mGy for the right forearm, and 12.5 mGy for the left forearm. The 2D dose distribution can be observed in figure 9, where again, one can observe the non-uniformity of the dose distribution due to the partial scan angle used for the HR-pQCT scanning procedure. The planar dose gradient along a line profile in the bone was found to be as high as 1.68 mGy · mm$^{-1}$, corresponding to a relative maximum variation of 160% along the profile.

Although not shown here for brevity, a linear profile of the in-plane dose map across the radius and ulna shows the dose decrease from one side to the opposite, and from the periphery to the center of the phantom (due to the shielding of surrounding tissues, originating a cup profile). Local maxima of the absorbed dose were found in the cortical bone of the radius in the upper side of the phantom (maximum value, 72.6 mGy). In the axial direction, we found a relative percentage variation of about 3% with respect to the mean value, for both the left and right forearms. The 3D dose map of the wrist was subdivided into individual dose maps

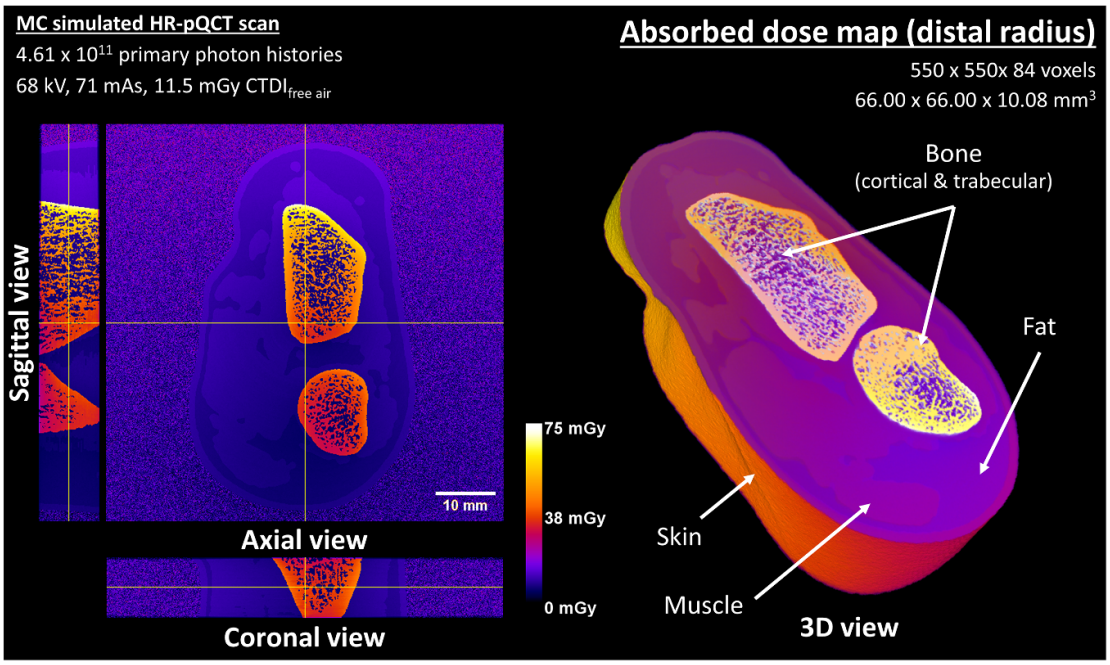


**Figure 9.** Axial, coronal, and sagittal views in a central slice of the 3D map of absorbed dose (mGy) derived from the MC simulation of a clinical HR-pQCT scan of a wrist. The partial angular scan (202°) produces a higher exposure of the upper part of the phantom, determining the higher dose levels seen in the upper part of the axial and in the 3D view. The dose scale shown refers to the three CT views only.

for each tissue (figure 10), from which average tissue doses were derived (table 4). We observed that, in this case, the highest absorbing tissue was the bone, with mean absorbed doses at 38.3 mGy and 38.6 mGy for the right and left bones, respectively. As done for the tibia, we computed the absorbed dose in the radius endosteum following the ICRP 116 Annex D (ICRP 2010)(section 2.8). From figure 2(d) in ICRP 116 Annex D, we used the factor at 40 keV, i.e $6 \times 10^{-17}$ Gy · m$^2$. Correspondingly, by considering a bone surface of $6.4 \times 10^{-4}$ m$^2$ for the radius (measured from the radius digital phantom), and a calculated incident photon fluence of $7.3 \times 10^{14}$ m$^{-2}$, we estimated an average absorbed dose to the radius endosteum of 43 mGy.

### 3.4. Effective dose estimates

From the absorbed dose maps and the corresponding mean absorbed doses in the tissues, we derived an estimate of the effective dose (equation (5)) for an HR-pQCT examination of the tibia and radius. Following the ICRP 103 recommendations, adipose tissue was excluded from the effective dose calculation, as the risk of radiation-induced cancer for adipose tissue is considered negligible (ICRP 2007).

Similar considerations apply to YBM, which is primarily composed of adipose cells, thus not considered a sensitive target. However, here we report effective dose estimates both with and without the contribution of YBM: the former represents a more conservative estimate, while the latter is more accurate for adult patients, for whom the epiphyses of long bones are generally not active bone marrow sites (Zankl *et al* 2007). These considerations do not apply to paediatric patients, as their long bones contain red bone marrow in the medullary cavities. Dose estimates excluding the YBM are reported in table 5, together with the contribution of each tissue to the effective dose.

Estimates of the effective dose, including the YBM as a target, were 2.05 $\mu$Sv and 2.13 $\mu$Sv for the right and left tibia, respectively, with an uncertainty of 36.06% (0.06% Type A uncertainty from MC simulation, plus 36% Type B uncertainty, see Supplementary material). For a radius HR-pQCT examination, effective doses were 1.48 $\mu$Sv and 1.49 $\mu$Sv for the right and left side, respectively, with an uncertainty of 39.06% (0.06% Type A uncertainty from MC simulation, plus 39% Type B uncertainty, see Supplementary material).

From the MC-estimated effective dose and the measured DLP, we computed also the effective dose conversion factors. By averaging the *k-factors* for the right and left limbs, we obtained an average *k-factor* of 0.185 $\mu$Sv ·mGy$^{-1}$ · cm$^{-1}$ for the tibia, and 0.133 $\mu$Sv · mGy$^{-1}$ · cm$^{-1}$ for the radius.

### 3.5. Influence of the segmentation thresholds on the dose estimates

We evaluated the influence of the threshold choice on the dose estimate, by repeating the MC simulations and effective dose calculations for two cases: one, using the left tibia phantom obtained by segmenting the

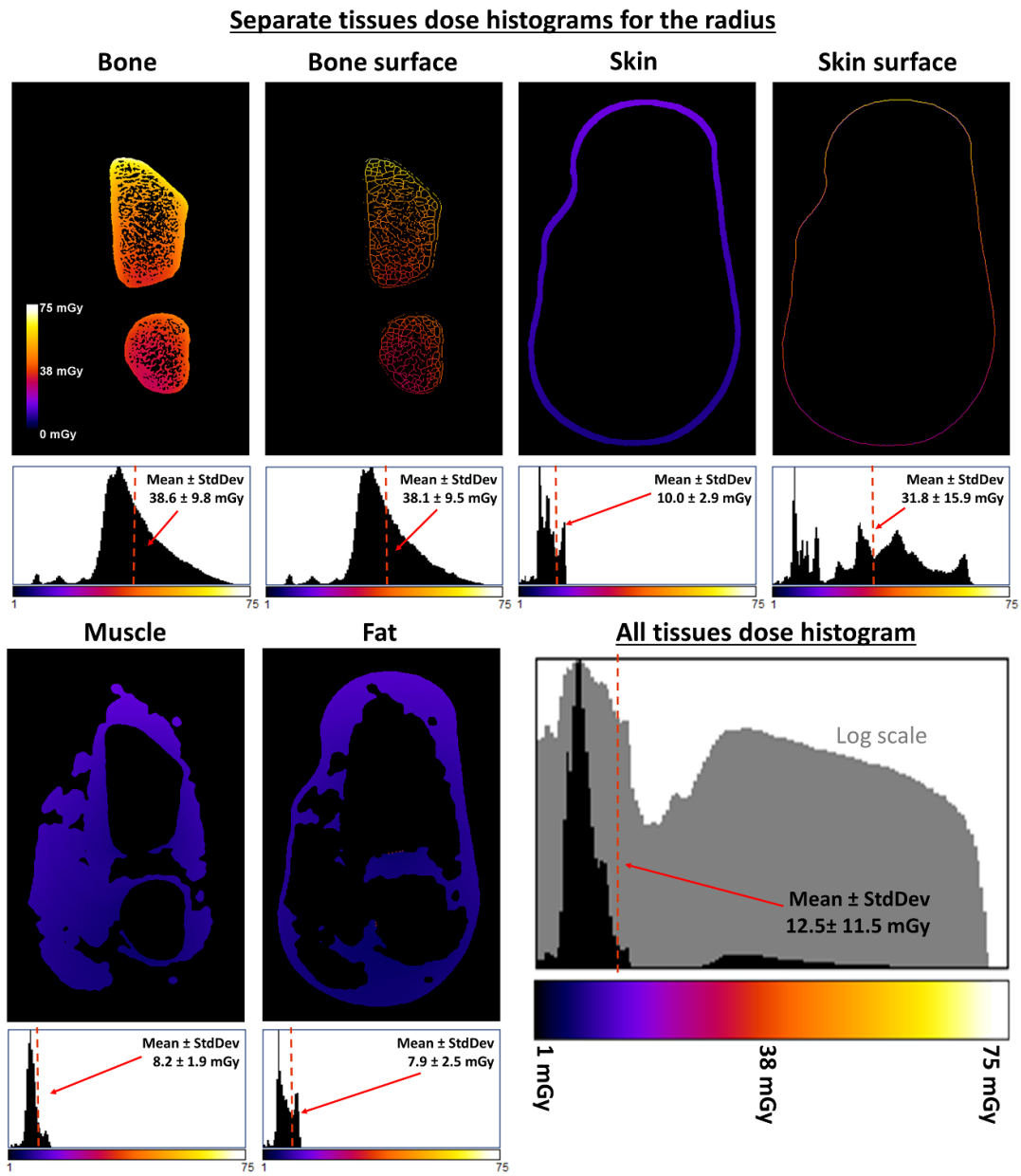


**Figure 10.** Absorbed dose maps (mGy) in the four separate tissues (bone, muscle, fat, and skin) of the radius with the relative histograms. The histogram of the absorbed dose in the whole phantom (excluding the air surrounding it) is also shown.

original images with lower threshold values, and the other, using the recommended (higher) thresholds. Table 6 shows the effective dose estimates obtained using a bone segmentation threshold of 320 mg HA · cm$^{-3}$, as suggested by the HR-pQCT guidelines (Whittier *et al* 2020) for trabecular bone in the left tibia, compared to the lower threshold (70 mg HA · cm$^{-3}$) adopted in this work for all simulations.

The higher thresholds determine a higher effective dose (3.20 $\mu$Sv), i.e. an increase of 50%. The largest contribution to this discrepancy is given by the YBM component, as both its mass fraction and the absorbed dose increase. This is also evident from the absorbed dose maps shown in figure 11, where the dose to the YBM is considerably higher for the segmentation performed using the recommended thresholds (figure 11(a)), with a ratio of average absorbed doses of 1.28 (i.e. a 28% increase, figure 11(d)) for the bone marrow, and of 1.20 (a 20% increase, figure 11(h)) in the case of bone tissue. However, if the YBM contribution is excluded from the effective dose estimate, the values for the two different threshold choices are compatible within uncertainties.

### 3.6. Computation time

The total duration of a MC simulation in this work was ∼43 min, including images writing time, with ∼4.66 × 10$^9$ photons being launched in total (∼4.6 × 10$^8$ per projection, with a total of 1011 projections).

**Table 5.** Effective doses for the HR-pQCT examination of the tibia and radius. Tissue weighting factors were taken from ICRP 103 (ICRP 2007). The statistical uncertainty on the effective dose estimates is 0.06% ($k = 3$). Values in parenthesis indicate the percentage contribution of each tissue to the total effective dose. Data reported in this table is derived for the phantoms obtained using a segmentation threshold of 70 mg HA · $cm^{-3}$ for the trabecular bone and of 200 mg HA · $cm^{-3}$ for the bone contour. Also reported are the calculated *E*/DLP dose coefficients.

| Right Tibia | | | | |
|---|---|---|---|---|
| | $w_T$ | Avg. absorbed dose (mGy) | Irradiated fraction $f_T$ | Contribution to the effective dose ($\mu$Sv) |
| Bone surface | 0.01 | 26.6 | 0.0010 | 0.27 (13.1%) |
| Skin surface | 0.01 | 27.8 | 0.0014 | 0.38 (18.4%) |
| Muscle | 0.12 | 6.1 | 0.0009 | 0.65 (31.7%) |
| Fat | 0 | 6.7 | 0.0011 | 0 (0%) |
| YBM | 0.12 | 4.2 | 0.0015 | 0.76 (36.8%) |
| Effective dose, $E$ ($\mu$Sv) | | | | 2.05 (100%) |
| Effective dose conversion coefficient $E/DLP$ ($\mu$Sv · $mGy^{-1}$ · $cm^{-1}$) | | | | 0.183 |
| Effective dose w/o YBM ($\mu$Sv) | | | | 1.30 |
| Left Tibia | | | | |
| | $w_T$ | Avg. absorbed dose (mGy) | Irradiated fraction $f_T$ | Contribution to the effective dose ($\mu$Sv) |
| Bone surface | 0.01 | 27.5 | 0.0010 | 0.27 (12.6%) |
| Skin surface | 0.01 | 27.8 | 0.0014 | 0.38 (17.9%) |
| Muscle | 0.12 | 6.1 | 0.0009 | 0.68 (31.9%) |
| Fat | 0 | 6.8 | 0.0010 | 0 (0%) |
| YBM | 0.12 | 4.4 | 0.0015 | 0.80 (37.6%) |
| Effective dose, $E$ ($\mu$Sv) | | | | 2.13 (100%) |
| Effective dose conversion coefficient $E$/DLP ($\mu$Sv · $mGy^{-1}$ · $cm^{-1}$) | | | | 0.190 |
| Effective Dose w/o YBM ($\mu$Sv) | | | | 1.33 |
| Right radius | | | | |
| | $w_T$ | Avg. absorbed dose (mGy) | Irradiated fraction $f_T$ | Contribution to the effective dose ($\mu$Sv) |
| Bone surface | 0.01 | 38.8 | 0.0006 | 0.22 (14.9%) |
| Skin surface | 0.01 | 31.7 | 0.0009 | 0.28 (19.2%) |
| Muscle | 0.12 | 8.2 | 0.0004 | 0.42 (28.6%) |
| Fat | 0 | 7.9 | 0.0004 | 0 (0%) |
| YBM | 0.12 | 6.2 | 0.0008 | 0.55 (37.3%) |
| Effective dose, $E$ ($\mu$Sv) | | | | 1.48 (100%) |
| Effective dose conversion coefficient $E/DLP$ ($\mu$Sv · $mGy^{-1}$ · $cm^{-1}$) | | | | 0.132 |
| Effective dose w/o YBM ($\mu$Sv) | | | | 0.93 |
| Left Radius | | | | |
| | $w_T$ | Avg. absorbed dose (mGy) | Irradiated fraction $f_T$ | Contribution to the effective dose ($\mu$Sv) |
| Bone surface | 0.01 | 38.6 | 0.0006 | 0.23 (15.7%) |
| Skin surface | 0.01 | 31.8 | 0.0009 | 0.29 (19.2%) |
| Muscle | 0.12 | 8.2 | 0.0004 | 0.43 (28.8%) |
| Fat | 0 | 7.9 | 0.0003 | 0 (0%) |
| YBM | 0.12 | 6.1 | 0.0007 | 0.54 (36.3%) |
| Effective dose, $E$ ($\mu$Sv) | | | | 1.49 (100%) |
| Effective dose conversion coefficient $E$/DLP ($\mu$Sv · $mGy^{-1}$ · $cm^{-1}$) | | | | 0.133 |
| Effective dose w/o YBM ($\mu$Sv) | | | | 0.95 |

**Table 6.** The average dose absorbed in tissues and effective dose obtained for the left tibia using a segmentation threshold of 70 and 200 mg HA · cm$^{-3}$ (left columns) and 320 and 450 mg HA · cm$^{-3}$ (right columns) to segment the trabecular and cortical bone. The statistical uncertainty on the effective dose estimates is 0.06% ($k = 3$).

| | Lower thresholds (this work) | | | Recommended thresholds[a] | | |
|---|---|---|---|---|---|---|
| Tissue | Avg. absorbed dose (mGy) | Irradiated fraction $f_T$ | Contribution to the effective dose ($\mu$Sv) | Avg. absorbed dose (mGy) | Irradiated fraction $f_T$ | Contribution to the effective dose ($\mu$Sv) |
| Bone surface | 27.5 | 0.0010 | 0.27 | 32.7 | 0.0011 | 0.35 |
| Skin surface | 27.8 | 0.0014 | 0.38 | 28.7 | 0.0014 | 0.39 |
| Muscle | 6.1 | 0.0009 | 0.68 | 6.4 | 0.0009 | 0.69 |
| Fat | 6.8 | 0.0010 | 0 | 6.9 | 0.0010 | 0 |
| YBM | 4.4 | 0.0015 | 0.80 | 5.4 | 0.0027 | 1.77 |
| Effective dose, $E$ ($\mu$Sv) | | | 2.13 | | | 3.20 |
| Effective dose w/o YBM ($\mu$Sv) | | | 1.33 | | | 1.43 |

[a] Whittier *et al* (2020).

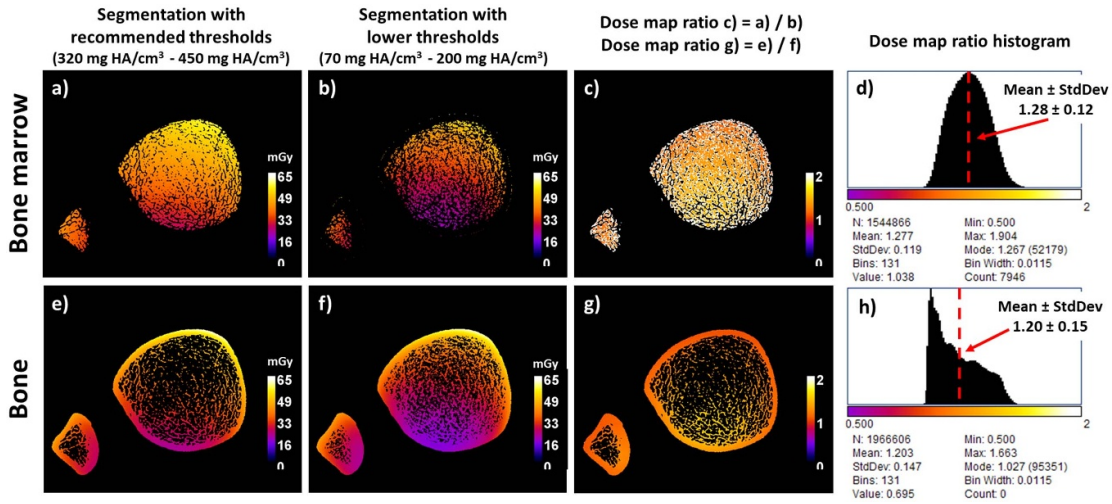


**Figure 11.** Comparison between the absorbed dose map in the bone marrow (a) and in the bone (e), obtained with the standard recommended thresholds (panels (a), (e)) and the ones obtained with the lower thresholds (panels (b), (f)). Images in panels (c) and (g) represent the ratio of the two dose maps and show that the dose in the phantom segmented with recommended thresholds is increased by 28% for the bone marrow and by 20% for the bone, on average, as shown in the dose map ratio histograms shown in panels (d) and (h), respectively.

The GPU computing time for a single projection is ∼450 ms, implying that the number of primary photons per second processed by our GPU-based MC code is ∼1 × 10$^9$, with a relative uncertainty of 0.06% ($k = 3$) on dose values, and digital voxelized phantoms with up to 50 million voxels. We measured that, by reducing the total number of primary photons by a factor of 100 (i.e. using only 4.6 × 10$^6$ photons per projection), the GPU time is reduced to ∼12 ms for a single projection, and ∼12 s for the complete CT simulation (corresponding to a GPU computational speed of 2.6 × 10$^9$ photons · s$^{-1}$), with a corresponding statistical uncertainty (3 × standard deviation of the mean) of 0.9% (see Supplementary materials figure S2 for details on this calculation). In this case, the total duration of the MC simulation (including hard disk access time) reduced to ∼37 min, with a reduction of 15% with respect to the previous case with a 100-times higher primary photons number.

## 4. Discussion

### 4.1. Tissue absorbed dose

The analysis of simulated absorbed dose maps within the examined anatomical regions revealed a marked non-uniform dose distribution produced by a HR-pQCT scan. This is attributable to the geometry of the irradiation procedure, which covers a scan angle of 202°, as opposed to the typical 360° scan angle used in conventional spiral CT scans. Future work will explore whether different irradiation geometries can produce a more uniform dose distribution, at a fixed average tissue dose; a specific investigated topic will be the dependence of the average tissue dose on the fixed starting angle in the rotation of the gantry.

In addition to computing the absorbed dose in the bone surface via dose maps, we computed the absorbed dose to the endosteum following recommendations by ICRP 116 (ICRP 2010), obtaining an absorbed dose of 27 mGy for the tibia and 43 mGy for the radius. These values are compatible, within the total uncertainties, with the average absorbed dose in the bone estimated from our simulation of 26.6–27.5 mGy for the tibia, and 38.8–38.6 mGy for the radius (table 5): the comparison indicates that the values we provided for the absorbed dose in the bone endosteum are not underestimated as a consequence of our choice of not considering the dose enhancement factors.

Using the software platform presented here—to be implemented with a description of the detector response—we will also investigate the effects on radiation dose and image quality produced by adopting a photon counting, energy selective detector in HR-pQCT. Indeed, this is the goal of an ongoing experimental project (Cerbone *et al* 2023a) which will employ CdTe based photon counting detectors of the Timepix4 series for DXA and HR-pQCT scans, Timepix4 being a microelectronic readout circuit recently tested by our group for nuclear medicine tasks (see Cerbone *et al* 2023b for details on the detector).

### 4.2. Effective dose estimate

The effective dose estimates obtained in this study for HR-pQCT examinations of the distal tibia (∼2 $\mu$Sv) and radius (∼1.5 $\mu$Sv) were lower than those reported by the manufacturer (3–5 $\mu$Sv), considering an estimated total uncertainty of about 40% (Type A + Type B uncertainties). Hence, one might regard the patient radiation level provided by the manufacturer as a conservative estimate. The highest contribution to the effective dose across all four examined scans comes from the YBM, contributing as much as 36%–37% of the total. The second most contributing tissue is the muscle (28%–32%), followed by the skin (18%–19%) and the bone surface, which only contributes 13%–16% to the effective dose of the scan.

We note that the YBM tissue might be excluded from the computation of the effective dose, as its main component is fat. However, we provided effective dose estimates both with and without YBM, considering the first as an upper bound for the effective dose value. Moreover, while it is true that, according to ICRP 89 (ICRP 2002), no red bone marrow is contained in the tibia and radius, and a 25 year-old female (i.e. the case of this work) is typically considered skeletally mature, individual variation should be considered. This is particularly relevant considering that 25 years represents the minimum age for skeletal maturity, and factors such as smoking, obesity, and participation in sports with a high oxygen debt may lead to the reconversion of YBM to red bone marrow (Małkiewicz and Dziedzic 2012). Consequently, it is conservative to account for the contribution of bone marrow to the effective dose in this specific case.

Finally, please note that the effective dose estimates reported in this work refer to a scan length of 10 mm at the distal tibia or radius. By increasing the scan length via consecutive adjacent scans—as normally adopted for increasing the scanner field of view—the corresponding effective dose will increase proportionally (without considering the scatter dose to adjacent tissue slabs; see, e.g. Mettivier *et al* (2016) for the details of the calculation method used for estimating the contribution of scatter dose in breast CT imaging with successive partial irradiations for covering the whole organ; see also Supplementary material for an estimate of scatter dose in this work).

### 4.3. MC simulation

The MC simulation platform developed in this work will be used in future works for the optimization of the dose with respect to the geometry of the scanner (scan angle, starting angular position of the scan) and the quality of the x-ray beam (analysis and optimization of the dose and quality of the image with a varying spectrum). Additionally, this MC software can be adapted to perform simulations of HR-pQCT scans of other skeletal sites such as the knee, which has lately become another site of interest for studying bone microarchitecture (Kroker *et al* 2017), and for which few estimates of the effective dose are available in the literature (50 $\mu$Sv, Kroker *et al* 2017).

The number of photons launched in these simulations was chosen to be as high as $4.6 \times 10^8$ photons per projection, to match the $CTDI_{100\text{-in-air}}$ measured on the clinical scanner, to obtain both the dose maps and the image projections (the latter were not analyzed in this work). This led to a statistical uncertainty of 0.06% ($k = 3$). However, by reducing the number of photons to $4.6 \times 10^6$ photons per projection, thus accepting a higher statistical uncertainty (0.9%, $k = 3$), the total computing time *per projection* could be reduced to only 12 ms GPU time, plus ∼800 ms for SSD disk saving of the sole dose map (for about 50 million voxels in the phantom). This paves the way for real-time, personalized dosimetry in HR-pQCT with our GPU-based MC code with less than 1% statistical uncertainty, which demonstrates a very relevant computing speed performance for a MC code running on a single GPU card.

We observe that the above-described computing performance is in line with our previous reports for GPU-accelerated MC virtual breast dosimetry (Mettivier *et al* 2022). Moreover, it is four orders of magnitude higher than a GEANT4 MC code for breast imaging running on a 16-core CPU cluster (di Franco *et al* 2020),

and 1–2 orders of magnitude better than what reported (though some years ago) for breast virtual dosimetry on a farm of (less performant) NVIDIA GeForce GTX 1080 GPU boards (Badal *et al* 2021).

### 4.4. Limitations

We point out that the density threshold used for the segmentation of trabecular bone from HR-pQCT images was 70 mg HA · $cm^{-3}$, while the value recommended by the HR-pQCT guidelines (Whittier *et al* 2020) is as high as 320 mg HA · $cm^{-3}$. At the same time, for the cortical tissue, we adopted a segmentation threshold of 200 mg HA · $cm^{-3}$, while the value suggested by the HR-pQCT scan guidelines is 450 mg HA · $cm^{-3}$. This produced a higher overall segmented bone volume (considering both the trabecular and the cortical bone tissues), which affects the determination of the mean absorbed dose in the bone and YBM and, in turn, the effective dose to the patient. A different effective dose estimate was, indeed, obtained using such thresholds (see section 3.5). In the MC simulations here reported, we used as digital phantom a single 10 mm thick slice of the distal tibia or radius, and we calculated the absorbed dose in the volume which is directly irradiated by the incident beam (collimated to 10 mm). However, this approach does not consider the scatter dose to adjacent tissue slices, which would give a contribution to the total effective dose. This may lead to an underestimation of both the fraction of irradiated organs and the average absorbed dose which, in turn, may lead to an underestimation of the effective dose (up to 30%, see Supplementary material).

Moreover, we assumed as negligible the absorbed dose for all organs that were not directly irradiated during the scan. We estimated that this assumption introduces a bias of 6% and 9% on the tibia and radius effective dose estimates, respectively. We therefore argue that the total relative uncertainty on our effective dose estimate should not exceed 40% (see Supplementary material).

Lastly, the geometry of the *in-silico* HR-pQCT scan was slightly different from the actual one, as the x-ray beam was axially collimated to 10 mm at the isocenter, while a collimation of 10.2 mm at the isocenter was set on the actual scanner, with a resulting slightly smaller irradiated volume in the simulation.

## 5. Conclusions

We presented a GPU-based MC software for estimating the absorbed and effective dose in adult patients HR-pQCT examinations of the distal tibia and radius. Effective doses for these examinations were less than 3 $\mu$Sv, compared with the manufacturer estimates in the range of 3–5 $\mu$Sv for such scans. We also provided, for the first time, effective dose to DLP conversion coefficients (*k-factors*) for HR-pQCT scans. This work will enable future dose optimization studies via analysis of alternative scanning geometries, energy spectrum selection and use of photon counting imaging detectors, to obtain a more accurate, optimized, real-time personalized estimate of the effective dose for HR-pQCT scans.

## Data availability statement

All data that support the findings of this study are included within the article (and any supplementary information files).

## Acknowledgment

L A C gratefully acknowledges the McCaig Institute team for hosting her and for the air kerma measurements on their clinical scanner, during her visit in Fall 2023. Thanks to Errol Steward (Alberta Health Services, Calgary, Alberta) for help during dosimetry measurements. L A C also acknowledges the Scuola Superiore Meridionale for funding her visit to the McCaig Institute, allowing her to acquire experimental data used in this work. The Timepix4 microelectronic readout circuit is realized by the Medipix4 collaboration (https://medipix.web.cern.ch/medipix4). Our virtual imaging and dosimetry platform (VIT-OSTEO) contributes to the INFN (Istituto Nazionale di Fisica Nucleare, Italy) project VITA (Virtual Imaging TriAls).

## Ethical statements

HR-pQCT scans of a volunteer used for this work were originally acquired for the Calgary Bone Health Study (CaBHS). The University of Calgary Conjoint Health Research Ethics Board approved the CaBHS study. All participants provided written informed consent. The research was conducted in accordance with the principles embodied in the Declaration of Helsinki and in accordance with local statutory requirements. Written informed consent was obtained from the subject involved in the study.

## ORCID iDs

Laura Antonia Cerbone https://orcid.org/0000-0002-9449-9927
Giovanni Mettivier https://orcid.org/0000-0001-6606-4304
Youfang Lai https://orcid.org/0000-0001-6940-9646
Xun Jia https://orcid.org/0000-0001-6159-2909
Steven K Boyd https://orcid.org/0000-0002-2930-5997
Paolo Russo https://orcid.org/0000-0001-9409-0008

## References

Abadi E *et al* 2024 Toward widespread use of virtual trials in medical imaging innovation and regulatory science *Med. Phys.* **51** 1–11
Adams J E 2009 Quantitative computed tomography *Eur. J. Radiol.* **71** 415–24
Badal A, Sharma D, Graff C G, Zeng R and Badano A 2021 Mammography and breast tomosynthesis simulator for virtual clinical trials *Comput. Phys. Commun.* **261** 10779
Bandirali M *et al* 2013 Dose absorption in lumbar and femoral dual-energy x-ray absorptiometry examinations using three different scan modalities: an anthropomorphic phantom study *J. Clin. Densitom.* **16** 279–82
Bazzocchi A, Ponti F, Albisinni U, Battista G and Guglielmi G 2016 DXA: technical aspects and application *Eur. J. Radiol.* **85** 1481–92
Berger M J, Coursey J S, Zucker M A and Chang J (NIST) 2005 ESTAR, PSTAR, and ASTAR: computer programs for calculating stopping-power and range tables for Electrons, Protons, and Helium Ions (version 2.0.1) (National Institute of Standards and Technology) (available at: https://physics.nist.gov/PhysRefData/Star/Text/ESTAR.html)(Accessed 01 2025)
Blake G M and Fogelman I 2007 The role of DXA bone density scans in the diagnosis and treatment of osteoporosis *J. Postgrad. Med.* **83** 509–17
Boone J M, McNitt-Gray M F and Hernandez A M 2017 Monte Carlo basics for radiation dose assessment in diagnostic radiology *J. Am. Coll. Radiol.* **14** 793–4
Boutroy S, Bouxsein M L, Munoz F and Delmas P D 2005 *In vivo* assessment of trabecular bone microarchitecture by high-resolution peripheral quantitative computed tomography *J. Clin. Endocrinol. Metab.* **90** 6508–15
Burrows M, Liu D and McKay H 2010 High-resolution peripheral QCT imaging of bone micro-structure in adolescents *Osteoporos. Int.* **21** 515–20
Cerbone L A, Cimmino L, Sarno A, Russo P, Sarno A, Biesuz N V, Bolzonella R, Mettivier G, Fiorini M and Russo P 2023b Monte Carlo and experimental evaluation of a Timepix4 compact gamma camera for coded aperture nuclear medicine imaging with depth resolution *Phys. Med.* **113** 102663
Cerbone L A, Russo P, Sarno A, Cimmino L and Mettivier G 2023a A prototype high-resolution peripheral quantitative CT scanner with photon counting detectors for bone loss assessment in osteoporosis *J. Bone Miner. Res.* **38** 224
Damilakis J, Adams J E, Guglielmi G and Link T M 2010 Radiation exposure in x-ray-based imaging techniques used in osteoporosis *Eur. Radiol.* **20** 2707–14
di Franco F, Sarno A, Mettivier G, Hernandez A M, Bliznakova K, Boone J M and Russo P 2020 GEANT4 Monte Carlo simulations for virtual clinical trials in breast x-ray imaging: proof of concept *Phys. Med.* **74** 133–42
El Maghraoui A and Roux C 2008 DXA scanning in clinical practice *Int. J. Med.* **101** 605–17
Gabel L, Liphardt A M, Hulme P A, Heer M, Zwart S R, Sibonga J D, Smith S M and Boyd S K 2022a Incomplete recovery of bone strength and trabecular microarchitecture at the distal tibia 1 year after return from long-duration spaceflight *Sci. Rep.* **12** 9446
Gabel L, Liphardt A M, Hulme P A, Heer M, Zwart S R, Sibonga J D, Smith S M and Boyd S K 2022b Pre-flight exercise and bone metabolism predict unloading-induced bone loss due to spaceflight *Br. J. Sports Med.* **56** 196–203
Gazzotti S, Aparisi Gómez M P, Schileo E, Taddei F, Sangiorgi L, Fusaro M, Miceli M, Guglielmi G and Bazzocchi A 2023 High-resolution peripheral quantitative computed tomography: research or clinical practice? *Br. J. Radiol.* **96** 20221016
Gong J K, Arnold J S and Cohn S H 1964 Composition of trabecular and cortical bone *Anat. Rec.* **149** 325–31
Huda W, Ogden K M and Khorasani M R 2008 Converting dose-length product to effective dose at CT *Radiology* **248** 995–1003
ICRP 2002 Basic anatomical and physiological data for use in radiological protection reference values ICRP publication 89 *Ann. ICRP* **32** (available at: www.icrp.org/publication.asp?id=icrp%20publication%2089)
ICRP 2007 The 2007 recommendations of the international commission on radiological protection ICRP publication 103 *Ann. ICRP* **37** 2–4 (available at: www.icrp.org/publication.asp?id=ICRP%20Publication%20103)
ICRP 2010 Conversion coefficients for radiological protection quantities for external radiation exposures. ICRP publication 116 *Ann. ICRP* **40** (available at: www.icrp.org/publication.asp?id=icrp%20publication%20116)
Ito M, Ikeda K, Nishiguchi M, Shindo H, Uetani M, Hosoi T and Orimo H 2005 Multi-detector row CT imaging of vertebral microstructure for evaluation of fracture risk *J. Bone Mineral Res.* **20** 1828–36
Jia X, Yan H, Cerviño L, Folkerts M and Jiang S B 2012a A GPU tool for efficient, accurate and realistic simulation of cone-beam CT projections *Med. Phys.* **39** 7368–78
Jia X, Yan H, Gu X and Jiang S B 2012b Fast Monte Carlo simulation for patient-specific CT/CBCT imaging dose calculation *Phys. Med. Biol.* **57** 577–90
Johnson P, Bahadori A, Eckerman K, Lee C and Bolch W E 2011 Response functions for computing absorbed dose to skeletal tissues from photon irradiation—an update *Phys. Med. Biol.* **56** 2347–65
Kemp T D, Besler B A, Gabel L and Boyd S K 2023 Predicting bone adaptation in astronauts during and after spaceflight *Life* **13** 2183
Kim S, Song H, Samei E, Yin F F and Yoshizumi T T 2011 Computed tomography dose index and dose length product for cone-beam CT: Monte Carlo simulations of a commercial system *J. Appl. Clin. Med. Phys.* **12** 84–95
Koivisto J, Kiljunen T, Kadesjö N, Shi X Q and Wolff J 2015 Effective radiation dose of a MSCT, two CBCT and one conventional radiography device in the ankle region *J. Foot Ankle Res.* **8** 8
Kroker A, Zhu Y, Manske S L, Barber R, Mohtadi N and Boyd S K 2017 Quantitative in vivo assessment of bone microarchitecture in the human knee using HR-pQCT *Bone* **97** 43–48
Krug R, Burghardt A J, Majumdar S and Link T M 2010 High resolution imaging techniques for the assessment of osteroporosis *Radiol. Clin. North Am.* **48** 601–21

Lee C, Lee C, Shah A and Bolch W 2006 An assessment of bone marrow and bone endosteum dosimetry methods for photon sources *Phys. Med. Biol.* **51** 5391–407
Link T M and Lang T F 2014 Axial QCT: clinical applications and new developments *J. Clin. Densitom.* **17** 438–48
Ludlow J B, Johnson B K and Ivanovic M 2018 Estimation of effective doses from MDCT and CBCT imaging of extremities *J. Radiol. Prot.* **38** 1371–83
Małkiewicz A and Dziedzic M 2012 Bone marrow reconversion—imaging of physiological changes in bone marrow *Pol. J. Radiol.* **77** 45–50
Manske S L, Zhu Y, Sandino C and Boyd S K 2015 Human trabecular bone microarchitecture can be assessed independently of density with second generation HR-pQCT *Bone* **79** 213–21
Mettivier G, Fedon C, Di Lillo F, Longo R, Sarno A, Tromba G and Russo P 2016 Glandular dose in breast computed tomography with synchrotron radiation *Phys. Med. Biol.* **61** 569–87
Mettivier G, Lai Y, Jia X and Russo P 2024 Virtual dosimetry study with three cone-beam breast computed tomography scanners using a fast GPU-based Monte Carlo code *Phys. Med. Biol.* **69** 045028
Mettivier G, Sarno A, Lai Y, Golosio B, Fanti V, Italiano M E, Jia X and Russo P 2022 Virtual clinical trials in 2D and 3D x-ray breast imaging and dosimetry: comparison of CPU-based and GPU-based Monte Carlo codes *Cancers* **14** 1027
Nishiyama K K and Shane E 2013 Clinical imaging of bone microarchitecture with HR-pQCT *Osteoporos. Int.* **24** 215–22
Poludniowski G, Omar A, Bujila R and Andreo P 2021 Technical note: spekpy v2.0—a software toolkit for modeling x-ray tube spectra *Med. Phys.* **48** 3630–7
Quintiens J, Coudyzer W, Bevers M, Vereecke E, van den Bergh J P, Manske S L and van Lenthe G H 2024 The quantification of bone mineral density using photon counting computed tomography and its implications for detecting bone remodeling *J. Bone Miner. Res.* **39** 1774–82
Scanco Medical 2015 XtremeCT II—user's guide, Rev. 2.4 TD-326 (Scanco Medical)
Schindelin J, Arganda-Carreras I, Frise E, Kaynig V, Longair M, Pietzsch T and Cardona A 2012 Fiji: an open-source platform for biological-image analysis *Nat. Methods* **9** 676–82
Sempau J, Acosta E, Baro J, Fernandez-Varea J M and Salvat F 1997 An algorithm for monte carlo simulation of coupled electron-photon transport *Nucl. Instrum. Methods Phys. Res.* B **132** 377–90
Thomas S R, Kalkwarf H J, Buckley D D and Heubi J E 2005 Effective dose of dual-energy x-ray absorptiometry scans in children as a function of age *J. Clin. Densitom.* **8** 415–22
Van den Bergh J P, Szulc P, Cheung A M, Bouxsein M, Engelke K and Chapurlat R 2021 The clinical application of high-resolution peripheral computed tomography (HR-pQCT) in adults: state of the art and future directions *Osteoporos. Int.* **32** 1465–85
Walters B R B, Kawrakow I and Rogers D W O 2002 History by history statistical estimators in the BEAM code system *Med. Phys.* **29** 2745–52
Whittier D E, Boyd S K, Burghardt A J, Paccou J, Ghasem-Zadeh A, Chapurlat R, Engelke K and Bouxsein M L 2020 Guidelines for the assessment of bone density and microarchitecture in vivo using high-resolution peripheral quantitative computed tomography *Osteoporos. Int.* **31** 1607–27
WHO 2004 World health organization scientific group on the assessment of osteoporosis at primary health care level *Summary Meeting Report*
Woodcock E, Murphy T, Hemmings P and Longworth S 1965 Techniques used in the GEM code for Monte Carlo neutronics calculations in reactors and other systems of complex geometry *Proc. Conf. Applications of Computing Methods to Reactor Problems* vol 557 (Argonne National Laboratory)
Yi Y, Lai C-J, Han T, Zhong Y, Shen Y, Liu X, Ge S, You Z, Wang T and Shaw C C 2011 Radiation doses in cone-beam breast computed tomography: a Monte Carlo simulation study *Med. Phys.* **38** 589–97
Zankl M, Eakins J, Gómez Ros J M and Huet C 2021 The ICRP recommended methods of red bone marrow dosimetry *Radiat. Meas.* **146** 106611
Zankl M, Eckerman K F and Bolch W E 2007 Voxel-based models representing the male and female ICRP reference adult—the skeleton *Radiat. Prot. Dosim.* **127** 174–86